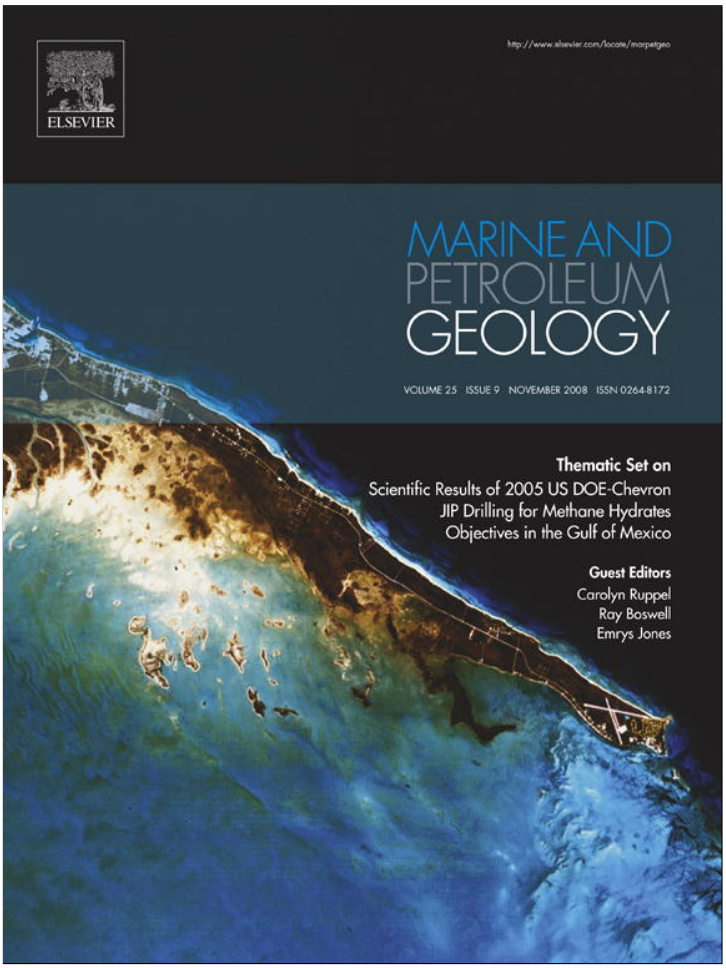

Marine and Petroleum Geology 25 (2008) 884–895

Contents lists available at ScienceDirect

Marine and Petroleum Geology

journal homepage: www.elsevier.com/locate/marpetgeo

Mechanical and electromagnetic properties of northern Gulf of Mexico sediments with and without THF hydrates

J.Y. Lee [a,1], J.C. Santamarina [a,2], C. Ruppel [b,*]

[a] School of Civil and Environmental Engineering, Georgia Institute of Technology, 790 Atlantic Avenue NW, Atlanta, GA, USA
[b] U.S. Geological Survey, 384 Woods Hole Road, Woods Hole, MA 02543, USA

ARTICLE INFO

Article history:
Received 31 January 2007
Received in revised form 12 October 2007
Accepted 14 January 2008

Keywords:
Gulf of Mexico
Gas hydrate
Permittivity
Conductivity
Fabric
Stiffness
Seismic velocity

ABSTRACT

Using an oedometer cell instrumented to measure the evolution of electromagnetic properties, small strain stiffness, and temperature, we conducted consolidation tests on sediments recovered during drilling in the northern Gulf of Mexico at the Atwater Valley and Keathley Canyon sites as part of the 2005 Chevron Joint Industry Project on Methane Hydrates. The tested specimens include both unremolded specimens (as recovered from the original core liner) and remolded sediments both without gas hydrate and with pore fluid exchanged to attain 100% synthetic (tetrahydrofuran) hydrate saturation at any stage of loading. Test results demonstrate the extent to which the electromagnetic and mechanical properties of hydrate-bearing marine sediments are governed by the vertical effective stress, stress history, porosity, hydrate saturation, fabric, ionic concentration of the pore fluid, and temperature. We also show how permittivity and electrical conductivity data can be used to estimate the evolution of hydrate volume fraction during formation. The gradual evolution of geophysical properties during hydrate formation probably reflects the slow increase in ionic concentration in the pore fluid due to ion exclusion in closed systems and the gradual decrease in average pore size in which the hydrate forms. During hydrate formation, the increase in S-wave velocity is delayed with respect to the decrease in permittivity, consistent with hydrate formation on mineral surfaces and subsequent crystal growth toward the pore space. No significant decementation/debonding occurred in 100% THF hydrate-saturated sediments during unloading, hence the probability of sampling hydrate-bearing sediments without disturbing the original sediment fabric is greatest for samples in which the gas hydrate is primarily responsible for maintaining the sediment fabric and for which the time between core retrieval and restoration of in situ effective stress in the laboratory is minimized. In evaluating the impact of core retrieval on specimen properties, it is also important to consider how far removed hydrate-bearing samples are from hydrate stability conditions.

1. Introduction

The impact of ice on the physical properties of host sediments has long been a subject of intense research in the geotechnical literature, but only in recent years has there been a major focus on understanding the properties of sediments containing another frozen substance – gas hydrate (e.g., Francisca et al., 2005; Yun et al., 2006a,b, 2007). Gas hydrate consists of a hydrogen-bonded water lattice surrounding guest gas molecules of low molecular weight. Methane is the most common guest molecule, but higher order hydrocarbons, hydrogen sulfide, and carbon dioxide also form gas hydrates under appropriate pressure and temperature conditions. Compared to ice, which persists only in permafrost regions, gas hydrates are far more widespread, occurring in both permafrost sediments to depths of ~1 km and deep marine sediments at water depths greater than ~300 m on the world's continental margins.

Scientific motivations for studying gas hydrates include their potential as an unconventional hydrocarbon resource, their possible role in global climate change, and/or their connection to seafloor geohazards such as slope failures. Laboratory studies comparing the geotechnical and geophysical properties of natural sediments both with and without gas hydrate advance our understanding of these issues in several ways. The resulting data could be used to calibrate relationships between geophysical parameters and gas hydrate saturation. Such relationships can be applied to evaluate the impact of hydrate formation and

* Corresponding author. Tel.: +1 508 457 2339.
E-mail addresses: jylee@kis.kigam.re.kr (J.Y. Lee), carlos@ce.gatech.edu (J.C. Santamarina), cruppel@usgs.gov (C. Ruppel).
[1] Present address: Korean Institute of Geoscience and Mineral Resources KIGAM, South Korea.
[2] Tel.: +1 404 894 7605.

0264-8172/$ – see front matter © 2008 Elsevier Ltd. All rights reserved.
doi:10.1016/j.marpetgeo.2008.01.019

dissociation on the mechanical behavior of hydrate-bearing sediments and to assess how coring and drilling of hydrate-bearing sediments affect their properties, an important issue for evaluating production strategies.

In this paper, we report on the geophysical and geotechnical properties of natural sediments obtained during conventional coring of boreholes drilled in potential gas hydrate zones in the northern Gulf of Mexico. The specimens were studied in both their undisturbed and remolded states, with and without synthetic hydrate. Results provide insight into processes accompanying the nucleation and growth of gas hydrate, new approaches to estimating hydrate saturation using geophysical observables, and the impact of coring on hydrate-bearing sediments.

2. Study site

Specimens for this study were obtained during 2005 drilling by the ChevronTexaco Joint Industry Project (JIP) on Methane Hydrates at two sites in the northern Gulf of Mexico (Fig. 1). The northern Gulf of Mexico seaward of the shelf break and north of the Sigbee escarpment is a complex passive margin setting characterized by a variable-thickness sedimentary section overlying deformed, allochthonous salt deposits. Salt dissolution and withdrawal have led to the formation of sediment-filled mini-basins, which mostly occupy bathymetric lows, surrounded by bathymetric highs that correspond to subsurface salt (e.g., Diegel et al., 1995; Peel et al., 1995). Faults that accommodate the rising salt play an important role in focusing fluid flow at the edges of mini-basins. Such faults often channel thermogenic gases upward toward the seafloor from deep hydrocarbon reservoirs (e.g., Sassen et al., 1999), leading to gas hydrate formation in shallow subseafloor sediments and occasionally at the seafloor when appropriate pressure–temperature conditions are encountered by the ascending fluids. At other locations, including the sites discussed in this paper, biogenic gas prevails (Lorenson et al., 2008). This gas may either represent migrated, older gas that has accumulated within the deeper sedimentary section or possibly biogenic gas generated in situ.

The two focus sites for the 2005 JIP drilling were Atwater Valley lease block 13 (AT13 at 28°N, 89.289°W and water depth of 1291 m) and Keathley Canyon lease block 151 (KC151-3 at 26.823°N, 92.987°W and water depth of 1323 m). Detailed descriptions of these sites are given elsewhere (e.g., Hutchinson et al., 2008; Wood et al., 2008), and initial results gleaned from drilling are detailed by Claypool (2006). The Keathley Canyon site lies on a bathymetric high close to a fault system on the southeastern side of the so-called Casey mini-basin, where a bottom simulating reflector (BSR) has been imaged (e.g., Hutchinson et al., in press). Drilling at the Atwater Valley site primarily focused on seafloor features identified before the cruise as possible gas hydrate mounds, but also included some reference sites outside the mound area. The AT13 sample analyzed in this paper was obtained at one of the reference sites. The KC and AT drilling sites represent different endmembers in the spectrum from a low flux gas hydrate site characterized by a BSR (KC151) to high flux site with punctuated fluid flow at the gas hydrate mounds (AT13). At the same time, the sites also lie at approximately the same water depth (hydrostatic pressure), which facilitates comparison of the hydrate stability conditions.

3. Sample description

Geotechnical and physical property results obtained on conventional (Yun et al., 2006a) and pressure cores (Yun et al., 2006b) recovered at the KC151 and AT13 sites have been previously documented in the literature. Data reported by Yun et al. (2006a) indicate that the specific surface S_a of the sediments at these sites varies from 62 $m^2 g^{-1}$ to 143 $m^2 g^{-1}$ in samples obtained from the uppermost ~150 m of sediments at AT13 and ~350 m at KC151. Such a high S_a suggests that the sediments are clay-dominated and likely indicates the presence of illite or/and montmorillonite. Based on the liquid limit LL (74.9–77.0 at AT13 and 51.2–66.6 at KC151) and the plastic limit PL (27.0–30.5 at AT13 and 20.7–22.7 at KC151), these sediments are classified as inorganic clays with high plasticity, corresponding to designator CH in the Unified Soil Classification System (Yun et al., 2006a). Results obtained more recently by Winters et al. (2008) on core materials from some of the same boreholes do not alter the conclusions published by Yun et al. (2006a) or the information summarized here.

For this study, we used whole-round samples obtained at 0.65 m below seafloor (mbsf) at AT13 (core AT13-1H) and 275 mbsf at KC151 (core KC151-3-19H). Both specimens were retrieved using the Fugro hydraulic piston corer. Conventional cores acquired at depths closest to the depths of our specimens have S_a of 94.2 $m^2 g^{-1}$ and 119.9 $m^2 g^{-1}$ and water content of 123.9% and 36.1% for AT13 and KC151, respectively (Yun et al., 2006a). Reported pore fluid salinities at these depths are 3.5% by weight at AT13 and between

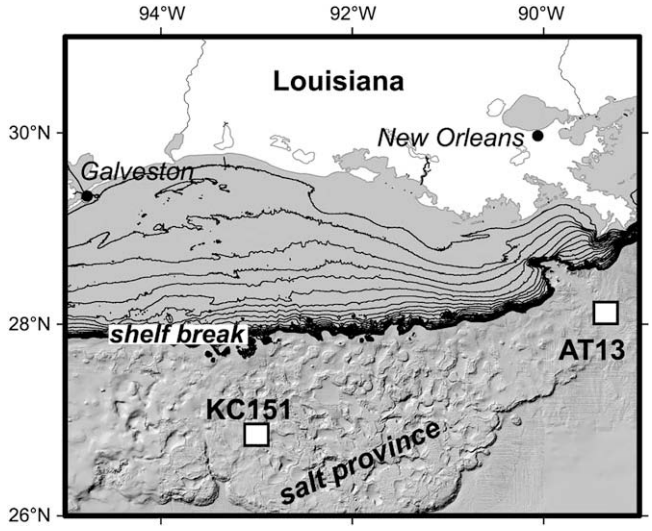

Fig. 1. Locations at which cores used in this study were recovered during 2005 DOE–JIP drilling in the northern Gulf of Mexico salt province.

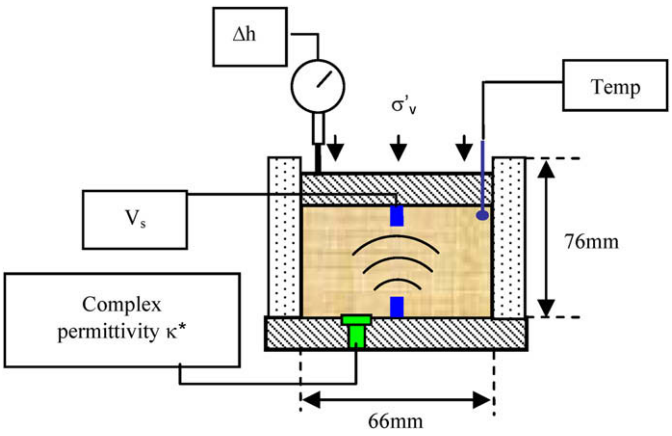

Fig. 2. Schematic of oedometer cell, sensors, and peripheral electronics. Temperature and complex permittivity sensors provide local measurements that average over only a small volume adjacent to the sensor. In contrast, the shear wave velocity represents a bulk, height-averaged value, primarily along the sample's axis.

Table 1
Results of oedometer tests on specimens from the northern Gulf of Mexico

Sample state	Sample	Pressure (MPa)	V_S (m s^{-1})	κ'	σ_{eff} (S m^{-1})	Void ratio
Undisturbed 0% of porosity filled by THF hydrate	AT13	0.00	20	50.28	2.28	3.07
		0.04	66	45.65	1.83	2.35
		0.10	90	42.31	1.73	1.72
		0.50	205	34.93	1.29	1.03
		1.18	328	33.31	1.06	0.78
		1.18	328	33.31	1.06	0.78
		0.50	310	33.81	1.11	0.79
		0.10	255	35.29	1.15	0.85
		0.04	179	37.68	1.32	0.97
		0.00	163	39.25	1.39	1.02
	KC151	0.00	171	27.07	1.25	0.96
		0.02	179	26.93	1.13	0.95
		0.10	209	26.79	1.09	0.83
		0.50	247	26.35	1.05	0.69
		1.14	290	25.72	1.00	0.60
		2.31	346	24.56	0.92	0.58
		2.31	346	24.56	0.92	0.58
		1.14	343	24.69	0.94	0.58
		0.50	330	24.88	0.95	0.59
		0.10	301	25.68	1.01	0.64
		0.02	282	25.81	1.01	0.66
		0.00	250	26.00	1.01	0.70
Remolded 0% of porosity filled by THF hydrate	AT13	0.00	41	40.58	1.84	2.01
		0.02	60	39.01	1.69	1.87
		0.10	127	36.05	1.47	1.40
		0.50	223	32.15	1.23	0.80
		1.18	247	28.70	1.05	0.56
		1.18	247	28.70	1.05	0.56
		0.50	247	28.94	1.05	0.59
		0.10	188	31.61	1.16	0.65
		0.02	132	32.00	1.17	0.77
		0.00	109	32.00	1.19	0.82
	KC151	0.00	45	35.58	2.01	1.74
		0.02	71	34.79	1.85	1.63
		0.10	119	34.69	1.80	1.33
		0.50	233	30.11	1.42	0.96
		1.18	310	27.18	1.20	0.75
		2.31	417	22.83	1.04	0.63
		2.31	417	22.83	1.04	0.63
		1.18	397	22.89	1.04	0.63
		0.50	302	23.20	1.07	0.64
		0.10	255	24.89	1.20	0.74
		0.02	173	26.36	1.32	0.80
		0.00	157	27.50	1.42	0.87
Remolded 100% of porosity filled by THF hydrate	AT13 frozen	0.00	Poor coupling	Poor coupling	Poor coupling	1.41
		0.02	1346	5.32	0.02	1.28
		0.10	1310	5.50	0.03	1.00
		0.50	1326	6.17	0.04	0.77
		1.18	1439	6.67	0.05	0.59
		1.18	1439	6.67	0.05	0.59
		0.50	1439	6.57	0.05	0.59
		0.10	1442	6.33	0.04	0.59
		0.02	1444	6.32	0.04	0.59
		0.00	1448	6.39	0.05	0.59
	AT13 unfrozen	0.00	51	Poor coupling	Poor coupling	1.41
		0.02	88	30.10	0.93	1.25
		0.10	137	29.36	0.91	0.95
		0.50	P-wave interference	26.79	0.77	0.77
		1.18	411	25.12	0.70	0.59
	KC151 frozen	0.00	Poor coupling	Poor coupling	Poor coupling	1.60
		0.02	1328	4.24	0.00	1.54
		0.10	1392	3.96	0.00	1.23
		0.50	1453	4.49	0.00	0.88
		1.18	1476	4.37	0.00	0.68
		2.31	1614	4.52	0.00	0.55
		2.31	1614	4.52	0.00	0.55
		1.18	1625	4.39	0.00	0.56
		0.50	1634	4.48	0.00	0.56
		0.10	1642	4.55	0.00	0.57

Table 1 (*continued*)

Sample state	Sample	Pressure (MPa)	V_S (m s^{-1})	κ'	σ_{eff} (S m^{-1})	Void ratio
		0.02	1644	4.55	0.00	0.57
		0.00	1648	4.55	0.00	0.57
	KC151 unfrozen	0.00	Poor coupling	Poor coupling	Poor coupling	1.60
		0.02	68	27.00	0.96	1.51
		0.10	136	27.50	1.09	1.21
		0.50	273	25.22	0.92	0.88
		1.18	363	22.61	0.77	0.67
		2.31	529	Lost calibration		0.54

5.0% and 5.3% by weight at KC151 (Kastner et al., 2008). The samples we tested were recovered from within the stability field for methane hydrate, and resistivity logs at 275 mbsf in KC151 also suggested the presence of gas hydrate in situ (e.g., Claypool, 2006; Lee and Collett, 2008). Nonetheless, we have no direct proof that gas hydrate was present in situ in the cores we tested.

4. Experimental design

This study was conducted using an instrumented oedometer cell to apply vertical effective stress to the sediment sample (7.62-cm high and 6.6-cm diameter) at zero-lateral strain (Fig. 2). The cell contains sensors to record complex permittivity κ^*, S-wave velocity V_S, volume change ε_{vol}, and temperature T. The cell's design permits all measurements to be conducted at steady state (constant temperature) as well as during formation and dissociation of synthetic hydrate (changing temperature).

A K-type thermocouple mounted through the top endcap of the cell is used to monitor the specimen temperature with a precision of 0.1 °C. Volume change is determined by tracking the instantaneous vertical position of the top cap using a linear variable displacement transducer (LVDT) with precision of 2.5×10^{-6} m.

Piezocrystal bender elements are used for S-wave measurements (Lee and Santamarina, 2005). The frequency content of the S-wave signal varies from 5 kHz to 70 kHz, depending on the sediment stiffness, which in turn reflects effective stress and/or

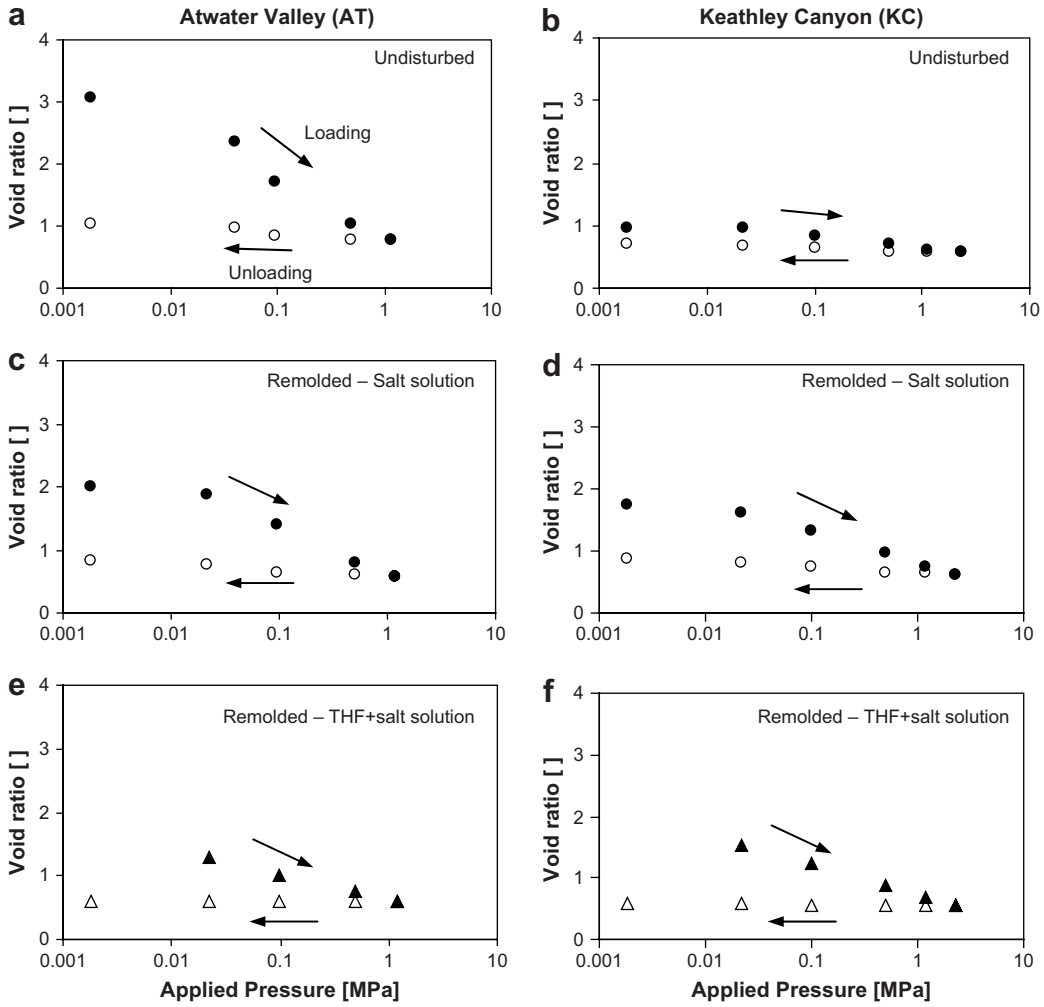

Fig. 3. Void ratio evolution during loading (solid symbols) and unloading (open symbols). All loading was applied while pore fluid was in the liquid phase. Circles indicate specimens lacking hydrates, and triangle show specimens with hydrates.

hydrate saturation. The source is housed in the bottom plate and connected to a signal generator, while the receiver bender element is mounted in the top cap and connected to a filter/amplifier. Both the signal generator and the filter/amplifier are connected to a storage oscilloscope that records data digitally.

The bottom plate houses the dielectric permittivity probe, which is connected to a computer-controlled network analyzer that measures the complex permittivity κ^* between 200 MHz and 1.3 GHz. Complex relative permittivity κ^* is given by $\kappa' + j\kappa''$, where κ' denotes the dielectric permittivity, $j^2 = -1$, and the imaginary component κ'' includes both conduction and polarization losses, the latter being considered negligible. The electrical conductivity σ_{el} is given by $\kappa''\varepsilon_0\omega$, where ε_0 is the permittivity of free space (8.854×10^{-12} F m^{-1}), and ω denotes angular frequency.

The oedometer cell, shown in Fig. 2, is placed in a lever-type gravity loading frame to facilitate stable, long-term loading. The cell, the loading frame, and peripheral electronics are housed in an environmental chamber at 4 °C. Temperature changes of the cell itself are imposed using dry ice pads and a heating pad.

4.1. Test procedure

The applied vertical effective stress σ'_v ranges from 0.01 to 1.2 MPa over four loading steps for the AT specimens and from 0.01 to 2.3 MPa over five loading steps for the KC specimens. This range of σ'_v covers not only the effective stress experienced by these specimens under in situ conditions, but also other stress conditions likely to prevail in shallow sediments of the northern Gulf of Mexico. Standard consolidation test procedure ASTM D2435 (ASTM, 2003) is followed during the tests for specimens without hydrates.

Specimens prepared for hydrate formation are subjected to additional steps. (1) Specimens are loaded at $T = 4$ °C without forming hydrates, with each loading step continuing until consolidation is complete; (2) the temperature is then reduced to induce complete hydrate formation; (3) the temperature is subsequently increased to provoke dissociation of all hydrate; and (4) a new loading step is applied. After the final loading step, the frozen specimen is unloaded to simulate core extraction in the field.

THF is selected as hydrate former for this study because of its complete miscibility with water and its capacity to form hydrate (Structure II) from the aqueous phase. A detailed discussion of advantages and disadvantages of using THF as hydrate former is presented in Lee et al. (2007). More information about THF hydrates and procedures adopted to counter experimental problems (e.g., evaporation) can be found in Yun et al. (2007) and Lee et al. (2007). Over the range of conditions used for these experiments, the hydrate formation process (e.g., ice seed, bubbling of gas, formation from dissolved phase) appears to have a greater impact on mechanical properties than does the specific hydrate former (e.g., THF vs. methane; Yun et al., 2007; Lee et al., 2007; Santamarina and Ruppel, 2008) or hydrate structure (e.g., Structure I vs. Structure II). In natural marine settings, methane hydrate within the hydrate stability zone probably forms primarily through the combination of water and aqueous phase methane (e.g., Hyndman and Spence, 1992; Zatsepina and Buffett, 2003).

4.2. Specimen preparation

The AT and KC specimens were tested under three different conditions.

- Undisturbed without hydrates. A 5 cm-thick core slice was placed in the oedometer cell within its original plastic core liner to prevent disturbance beyond that already associated with the acquisition of the core.
- Remolded without hydrates. The specimen was dried in an oven, ground in a mortar, and mixed with deionized water to the pre-drying water content. After the mixture reached the original water content and pore water salt concentration, a NaCl solution (3% by weight for AT13 and 5% by weight for KC151) was added until the soil–solution mixture attained a saturated, paste-like consistency. This process ensured liquid content close to the liquid limit and full saturation of the specimens. This preparation procedure was designed to destroy the soil structure while maintaining the pore fluid salt concentration close to the in situ conditions.
- Remolded with 100% hydrate pore saturation. Sediments were dried in an oven, ground with a mortar, and mixed with 20% by weight THF solution (stoichiometric solution for the THF hydrate) to the pre-drying water content. After the mixture reached the original water content and pore water salt

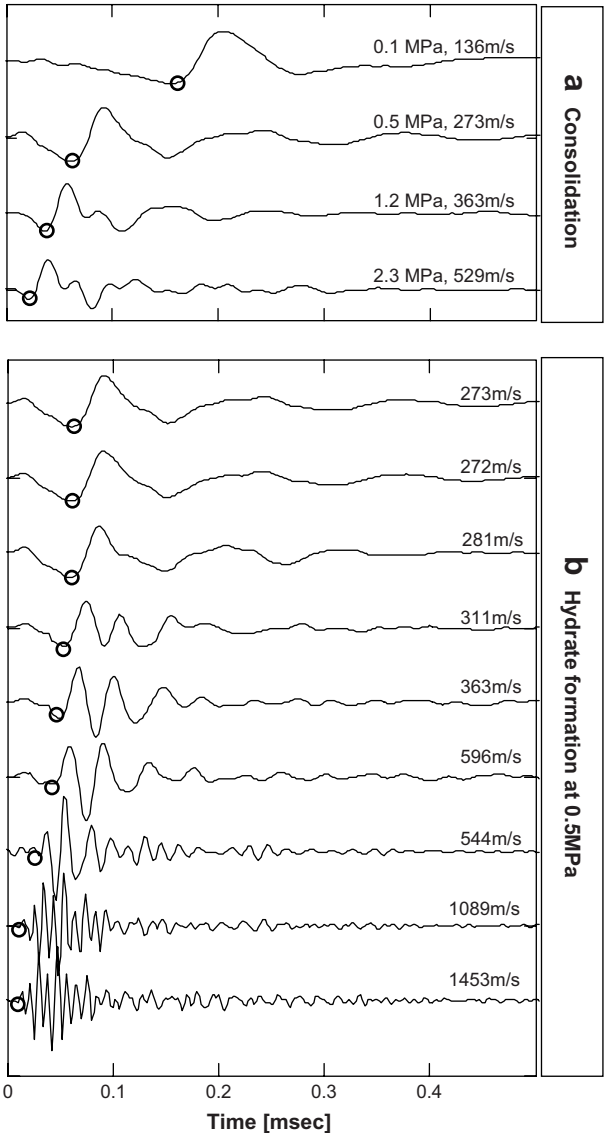

Fig. 4. Evolution of S-wave signatures gathered for KC specimen with 20% THF–salt solution in pore space (a) at the end of each loading step and (b) during phase transformation at 0.5 MPa. Circles on waveforms indicate first arrivals from which velocities were calculated. Note changes in the characteristics of the waveforms during hydrate formation.

concentration, a 20% THF solution with the appropriate salt concentration was added until the mixture exhibited a paste-like behavior consistent with these fine-grained sediments having reached their liquid limit, indicating full saturation of a specimen.

5. Results

This section provides an overview of the experimental results. Data from the experiments are shown in Table 1.

5.1. Volume change

Fig. 3 shows the void ratio after consolidation for each loading step for all six tests, during both loading and unloading. The initial void ratio for the undisturbed AT13 specimen was high ($e_0 = 3.07$), consistent with its shallow subseafloor depth. The pre-consolidation pressure estimated from the overburden is ~2.7 kPa, so the loading imposed during this experiment was virgin loading. The compression index C_c describes the slope of the normal consolidation line on a plot of void ratio vs. the logarithm of σ'_v, while the swelling index C_s or recompression index C_r refers to the slope of the unloading/reloading curves on the same type of plot. The AT13 sample has $C_c = 0.9$ and $C_s = 0.1$, confirming that the specimen is normally consolidated in its undisturbed state.

In contrast, the initial void ratio for the undisturbed KC151 specimen was low ($e_0 = 0.96$) since it was buried at ~275 mbsf. The estimated pre-consolidation pressure was ~2.3 MPa, so loads applied during this experiment were in the reloading branch ($C_r = 0.15$ and $C_s = 0.05$), and the measured volume changes were small in both loading and unloading.

By their very nature, remolded samples are inherently normally consolidated. The apparent pre-consolidation pressure (0.05 MPa) observed in Fig. 3 reflects the initial void ratio at the time of remolding.

5.2. S-wave velocity

Fig. 4a shows a selection of waveforms gathered at the end of each consolidation step and during phase transformation for the remolded KC151 specimen. The pattern of increasingly fast first arrivals indicates that the S-wave velocity is dependent on the effective stress, which plays a critical role in controlling the stiffness of uncemented sediments (Santamarina et al., 2001). However,

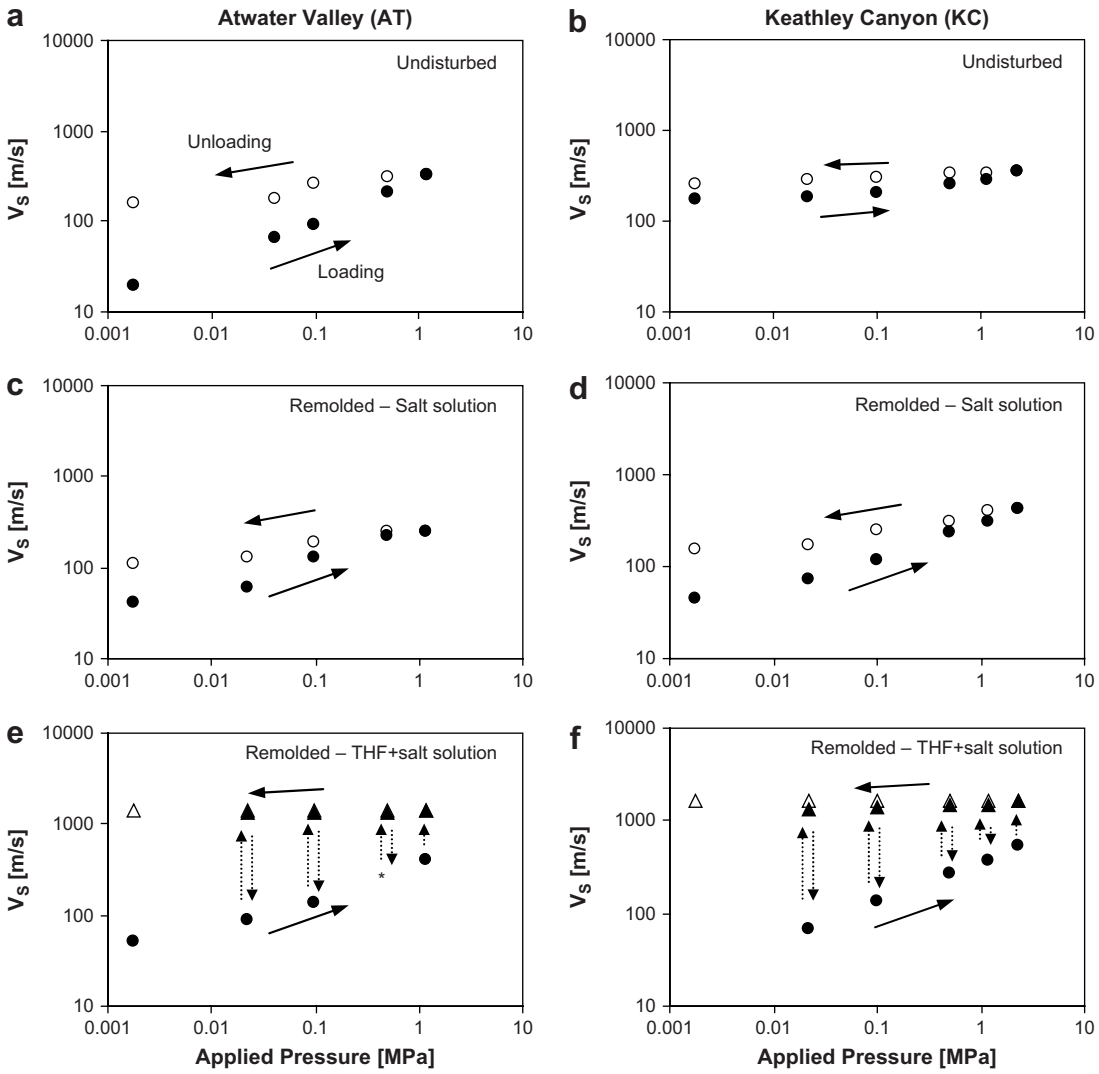

Fig. 5. S-wave velocity evolution during loading (solid symbols) and unloading (open symbols). An asterisk indicates interpolated data. Circles denote specimens lacking hydrates, and triangle shows specimens with hydrates.

Fig. 4b highlights another effect, namely the impact of hydrate formation on the stiffness of hydrate-bearing sediments held at constant effective stress.

These observations are further confirmed through analysis of the complete S-wave velocity data set shown in Fig. 5. Following a Hertzian-type formulation, V_S can be related to the mean stress in the polarization plane through

$$V_s = \alpha\left(\frac{\sigma'_v + K'_0\sigma'_v}{2\ \text{kPa}}\right)^{\beta}, \quad (1)$$

where K'_0 is the lateral earth pressure coefficient at zero-lateral strain, and α and β are experimentally determined coefficients. The constant α denotes V_S at $\sigma'_v = 1$ kPa, and the exponent β is a measure of the sensitivity of V_S to σ'_v.

The S-wave velocity in the undisturbed specimens without hydrates (Fig. 5a, b) increased with the applied vertical effective stress σ'_v with an exponent of $\beta = 0.1$ in the KC151 specimen within the reloading range. In the AT13 specimen, $\beta = 0.4$ due to the significant change in the coordination number (number of contacts per particle) during virgin loading. During vertical unloading, V_S decreased slightly in both specimens because high coordination and horizontal effective stress remained locked in.

The S-wave velocity of remolded specimens without hydrates (Fig. 5c, d) increased with increasing vertical effective stress with exponent $\beta \cong 0.3$ for both the KC and AT specimens. This result reflects the fact that remolded specimens are inherently normally consolidated. During unloading, the S-wave velocity in specimens decreased slightly, similar to the case of undisturbed specimens.

The S-wave velocity of remolded specimens in which we form hydrate (20% THF–salt pore fluid solution) increased markedly during each hydrate formation event (Fig. 5e, f). Importantly, the S-wave velocity for the specimen with nominal 100% hydrate saturation was nearly independent of the state of stress. Throughout this paper, we define hydrate saturation as the volume of voids filled with hydrates normalized by the total volume of voids.

After the completion of phase transformation at the final loading step ($\sigma'_v = 2.3$ MPa), the frozen specimens were unloaded to $\sigma'_v = 0$ Pa. Almost no decrease in V_S was observed during unloading, indicating that no significant decementation/debonding occurred in these fine-grained specimens with high hydrate concentration.

5.3. Permittivity and electrical conductivity

The electrical conductivity σ_{el} of fluid-saturated sediments is governed by the fluid-filled porosity n of the sediments and the conductivity of the pore fluid (i.e., ionic concentration and mobility). Surface conduction effects can be neglected in marine sediments (Klein and Santamarina, 2003). The dielectric permittivity κ' of soil–water mixtures in the microwave frequency range is dominated by the orientational polarization of free water molecules relative to their volume fraction in the soils. These physical principles provide insight into the permittivity and conductivity spectra shown in Fig. 6 for specimens at the end of each loading step and during phase transformation.

As the load increases or as the phase transformation proceeds, κ' decreases due to the decrease in the volume fraction of free water. At the same time, σ_{el}, which like κ' is measured at microwave frequencies and is sensitive only to changes in the vicinity of the sensor, decreases due to the decrease in porosity and ionic mobility. The decrease in κ' and the increase in σ_{el} with the increase in frequency are due to free water polarization in the microwave frequency range. These observations are further validated by the trends in permittivity and electrical conductivity data as a function of the vertical effective stress shown in Figs. 7 and 8.

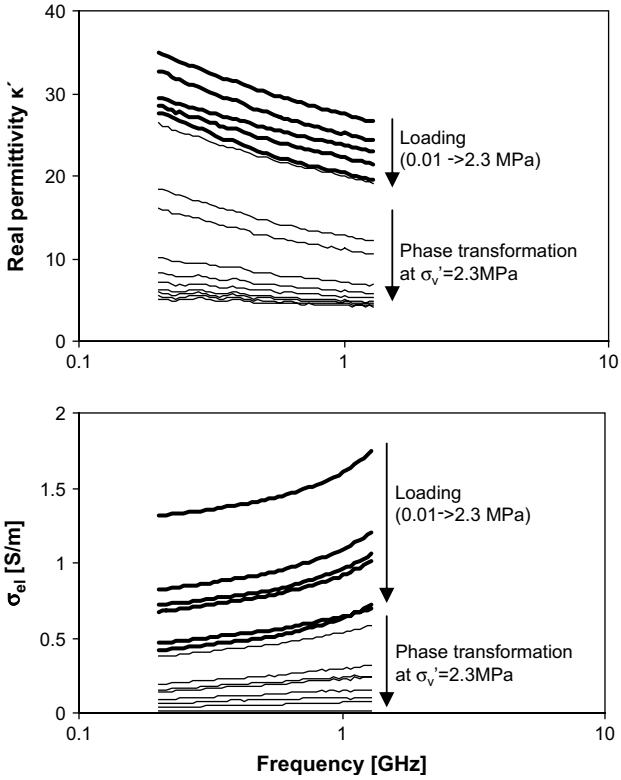

Fig. 6. Real permittivity and electrical conductivity spectra gathered for the KC specimen with 20% THF–salt pore fluid at the end of each loading step (0.01, 0.1, 0.5, 1.2, and 2.3 MPa) and during phase transformation after the final loading step (2.3 MPa). Thick lines correspond to measurements at the end of consolidation but before hydrate formation. The thin lines show the evolution of the spectrum during hydrate formation (after consolidation under 2.3 MPa).

As the vertical effective stress increases in specimens lacking hydrate, the real permittivity and the electrical conductivity decrease due to the decrease in void ratio (Fig. 3). Larger changes in the electrical properties imply larger changes in void ratio. The soft undisturbed AT13 specimen experienced a more pronounced drop in κ' and σ_{el} than the stiff undisturbed KC151 specimen.

Hydrate formation causes a pronounced decrease in permittivity, down to the range of non-polarizable materials (Fig. 7e, f). In contrast to sediments lacking hydrate, the real permittivity of hydrate-bearing sediments slightly increases as the vertical effective stress increases and the void ratio decreases (Fig. 7e, f). Two factors may contribute to this phenomenon. First, the fraction of unfrozen bounded water in a pore volume increases as free water drains and the porosity decreases under the higher vertical effective stress. Second, clay minerals, which make up a significant fraction of these specimens, have higher permittivity than THF hydrate. Electrical conductivity drops to undetectable, near-null values after hydrate formation (Fig. 8e, f).

5.4. Phase transformation

Fig. 9 shows a data set gathered for the KC specimen while subjected to $\sigma'_v = 1.2$ MPa. The temperature of the cell was gradually lowered to $-52\,^{\circ}C$ at a cooling rate of $\sim 0.5\,^{\circ}C\,min^{-1}$ by placing ground dry ice against the thick stainless steel cell wall. Although the geophysical signatures clearly indicate hydrate formation, no exothermic event was detected in the temperature data. The extremely low temperature attained during cooling caused the fast dissipation of the heat generated from exothermic hydrate formation. During hydrate formation, the S-wave velocity increased

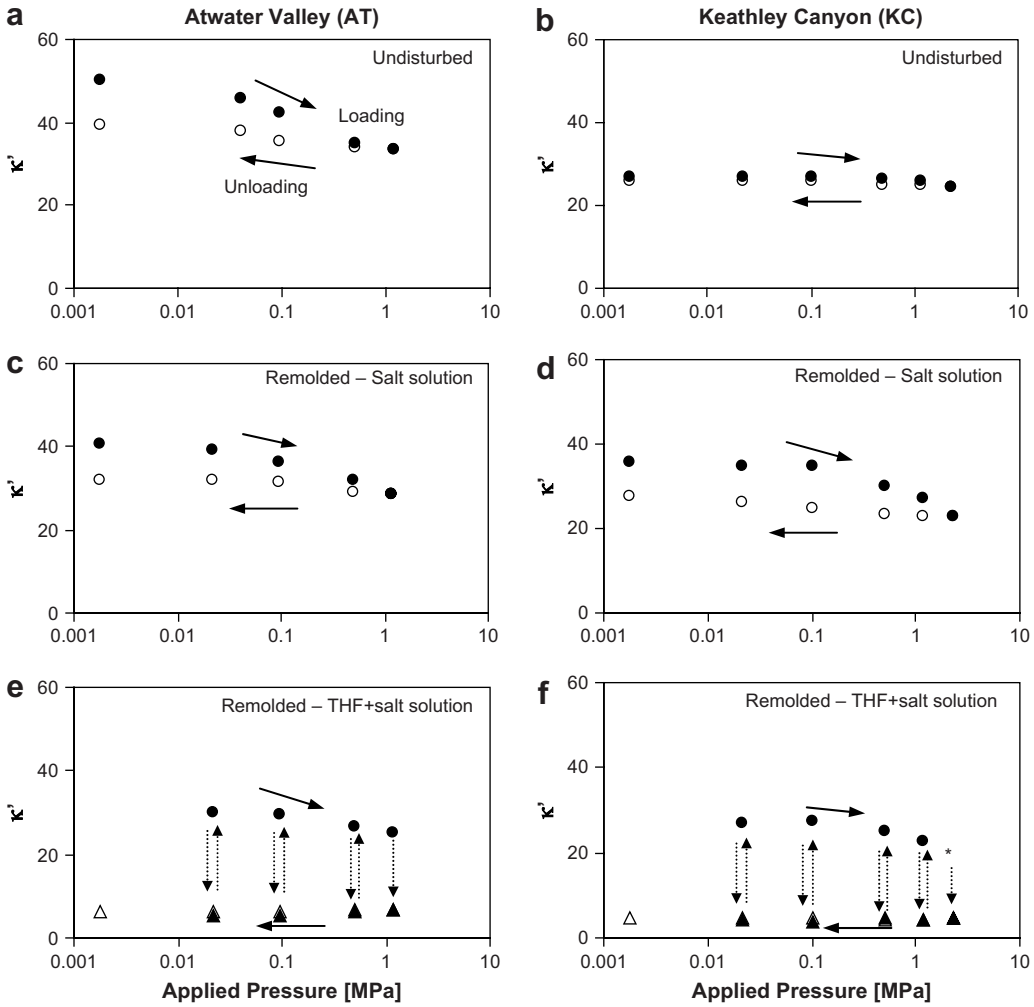

Fig. 7. Real permittivity during loading (solid symbols), phase transformation, and unloading (open symbols). Asterisk indicates interpolated missing data. Circles denote specimens lacking hydrates, and triangles indicate specimens with hydrates.

from 360 m s^{-1} to 1480 m s^{-1}, permittivity decreased from 23 to 5, and electrical conductivity decreased to undetectably low values (Table 1). Hysteresis between freezing and thawing was evident in all geophysical measurements when data were plotted vs. temperature. We also detected volume expansion of $\varepsilon_{vol} = 0.01$ during hydrate formation. Such volume expansion alters force equilibrium conditions at grain contacts and fundamentally perturbs the soil skeleton. During hydrate dissociation, we observed a corresponding residual settlement Δh_r related to the slight collapse of the soil skeleton that had been perturbed by volume expansion during hydrate formation.

6. Analysis and discussion

The initial porosity (related to C_c), mean pore size, and stiffness (related to V_S) of sediments are controlled by their loading history, particle shape, grain size distribution, cementation, packing, and specific surface. Following consolidation, a lower void ratio is attained in the specimens with the THF solution in the pore space than in the specimens with electrolytes. This is a consequence of the lower pore fluid polarizability, which leads to a thinner double layer and densification as a result of residual settlement after the end of the dissociation cycle.

The most important features in the S-wave velocity data are (a) stiffness that is highly dependent on stress in normally consolidated specimens without hydrates; (b) reduced stress dependence of stiffness in specimens within the preloaded range; and (c) stiffness that is independent of stress in specimens with 100% hydrate saturation. The last feature has been observed in previous studies of synthetic sediment specimens fully saturated with THF hydrate (Santamarina et al., 2004).

More importantly, permittivity and conductivity are good indicators of hydrate presence. The real permittivity in the microwave range is confirmed as a good indicator of volumetric free water content, capturing volume reduction of free water during consolidation and reduced water polarizability during hydrate formation. Electrical conductivity follows similar trends, but its response is governed by ionic concentration and ionic mobility.

6.1. Core sampling effects on hydrate-bearing sediment properties

The void ratio and S-wave velocity of sediments with 100% hydrate saturation show minimal change during unloading from $\sigma'_v = 1.2$ and 2.3 MPa to zero confinement. This indicates that the THF hydrate in pores can bind soil particles and resist the extensional deformation associated with stress relaxation. Results from a complementary set of experiments with both clay and sand specimens also showed lower void ratio change during the unloading of hydrate-bearing sediments than in the same sediments without hydrates (Lee, 2007). The stabilizing effect of

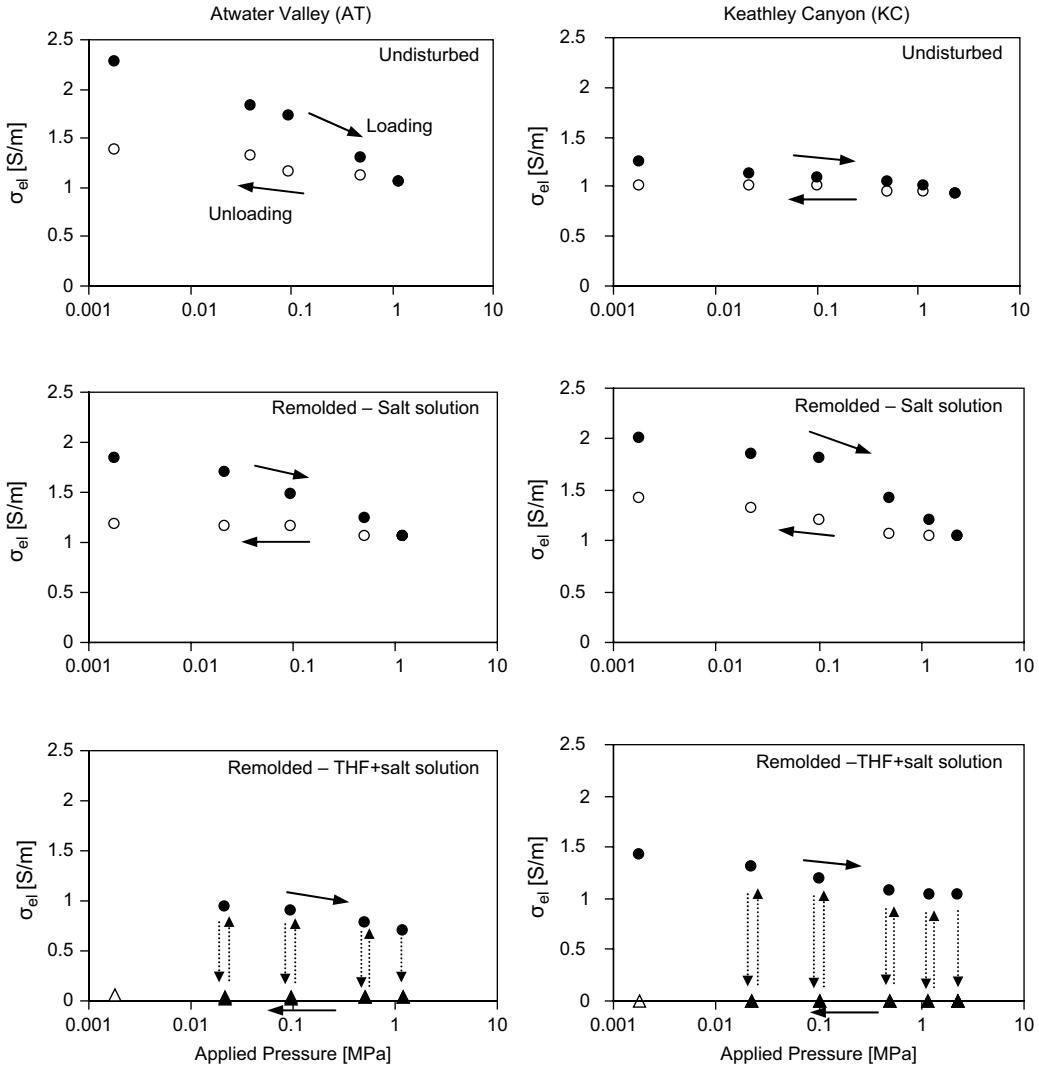

Fig. 8. Electrical conductivity during loading, phase transformation, and unloading. Circles indicate specimens lacking hydrates, and triangle indicates specimens with hydrates.

hydrates presumes that pore fluid pressure and temperature conditions are maintained within the hydrate stability field at the pore scale; however, the stretching of the granular skeleton will cause a decrease in the internal pore fluid pressure and tension in hydrates bonded to different grains. Therefore, future detailed analysis will be required.

6.2. Impact of hydrate formation on geophysical parameters

The gradual increase in V_S observed during hydrate formation (Fig. 9) indicates that hydrates do not form instantaneously throughout the specimen. Due to the placement of the source and receiver, the measured V_S data represent a height-averaged value, and the pattern of the increase in V_S during hydrate formation may in part reflect a non-homogeneous thermal field and the existence of a propagating freezing front. However, there are also gradual decreases in κ' and σ_{el}, and both of these parameters are averaged over a small volume adjacent to the sensor. Thus, these changes in local κ' and σ_{el} reflect gradual, rather than instantaneous, hydrate formation in pores. By slowly depressing the temperature of hydrate formation, two coexisting pore-scale phenomena can lead to such a pattern of changes in properties during hydrate formation. (1) Ion exclusion causes an increase in the ionic concentration of the remaining pore fluid in a closed system; and (2) gradually smaller pores remain unfrozen during hydrate formation due to pore size effects. Both effects contribute to the gradual depression of the equilibrium temperature and are analyzed next.

6.3. Effect of ionic concentration on hydrate equilibrium temperature

The depression of hydrate equilibrium temperature due to salt concentration can be estimated from the Hammerschmidt equation (Sloan, 1998). The activity of water a_w is related to the equilibrium temperature of gas hydrate phase transformation with salts T_s [K] and without salts T_w [K] through

$$\ln a_w = \frac{\Delta H}{NR}\left[\frac{1}{T_w} - \frac{1}{T_s}\right], \tag{2}$$

where ΔH is the heat of dissociation of THF hydrate (98 kJ mol^{-1}; Leaist et al., 1982), N is the hydrate number (17 for THF hydrate), and R denotes the universal gas constant (8.31 J K^{-1} mol^{-1}). The freezing temperatures of water with salts T_{fs} [K] and water without salts T_f [273.15 K] have a similar relationship with the activity of water

$$\ln a_w = \frac{\Delta H_{fus}}{R}\left[\frac{1}{T_f} - \frac{1}{T_{fs}}\right], \tag{3}$$

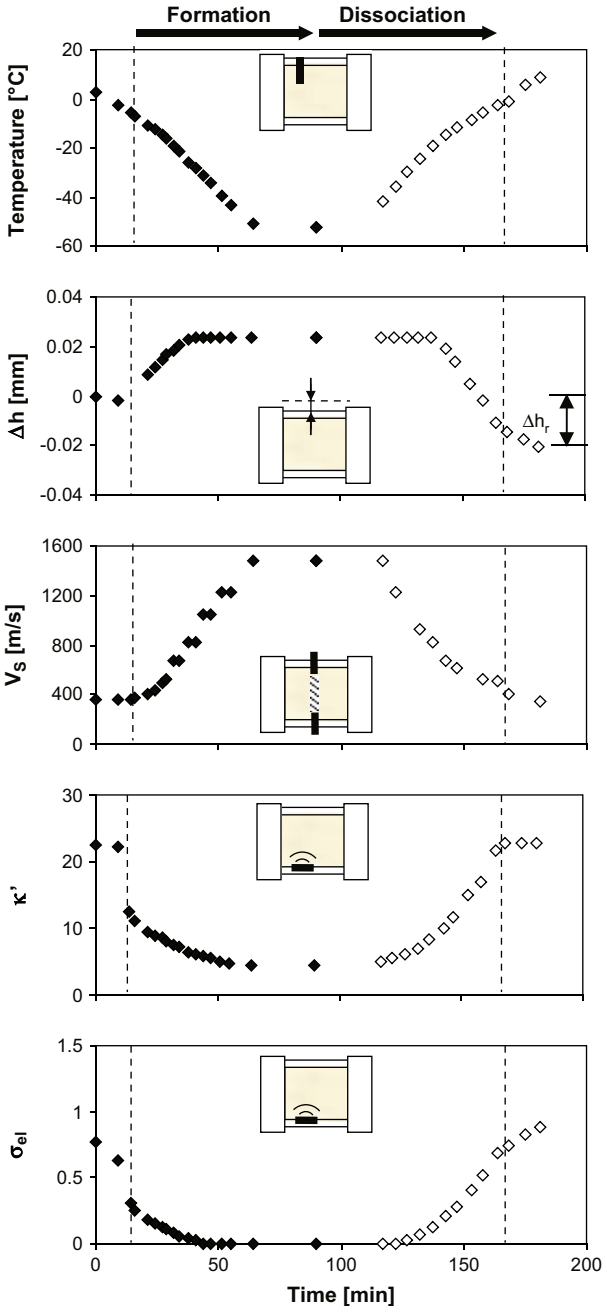

Fig. 9. Phase transformation in KC specimen subjected to the vertical effective stress $\sigma'_v = 1.2$ MPa. Vertical displacement ΔH and S-wave velocity V_S are global height-averaged measurements across the specimen. Temperature T, real permittivity κ', and electrical conductivity σ_{el} are local measurements. The schematic diagram in each graph illustrates the location of sensors. Dashed lines indicate the onset of hydrate formation and the end of hydrate dissociation.

where ΔH_{fus} [6008 J mol^{-1}] is the heat of fusion of ice. Combining these two equations leads to the equation for the equilibrium temperature of gas hydrate phase transformation in an electrolyte

$$\left[\frac{1}{T_w} - \frac{1}{T_s}\right] = \frac{\Delta H_{fus} N}{\Delta H}\left[\frac{1}{T_f} - \frac{1}{T_{fs}}\right]. \quad (4)$$

The freezing temperature T_{fs} of an electrolyte is obtained from Lide (2003). The equilibrium temperature T_w is 4.5 °C when the solution is stoichiometric. The estimated equilibrium temperature is 2.2 °C for the AT specimen with 0.53 molal of initial salt concentration in the pore fluid, and 0.9 °C for the KC specimen with 0.91 molal of initial salt concentration in the pore fluid. However, the equilibrium temperature drops to −16.6 °C for a salt-saturated (molality of 6) pore fluid.

6.4. Effect of pore size on hydrate equilibrium temperature

The formation of gas hydrate in porous media has a significant impact on hydrate nucleation and growth. First, the size of hydrate embryos can be restricted by sediment pore size. Second, hydrate growth is affected by capillary pressure (Everett, 1961; Clennell et al., 1999; Mullin, 2001). The equilibrium temperature depression ΔT_{pore} [K] related to capillary effects can be estimated with the Kelvin and the Clapeyron equations for a cylindrical pore with radius r [nm] (Anderson et al., 2003; Clennell et al., 1999)

$$\Delta T_{pore} = \frac{2\gamma_{sl} T_{bulk} \cos\theta}{\rho \Delta H r}, \quad (5)$$

where T_{bulk} [K] is the equilibrium temperature in bulk phase, γ_{sl} denotes the interfacial tension between hydrate and liquid (31 mJ m^{-2} for THF hydrate and water), θ represents the contact angle between hydrate and the pore wall ($\theta = 0°$ assuming unfrozen liquid layer at the pore wall), and $\rho = 970$ kg m^{-3} is the mass density of THF hydrate. Assuming that all plates of the mineral grains are parallel, the average separation r between platy particles can be estimated from the sediment specific surface S_a

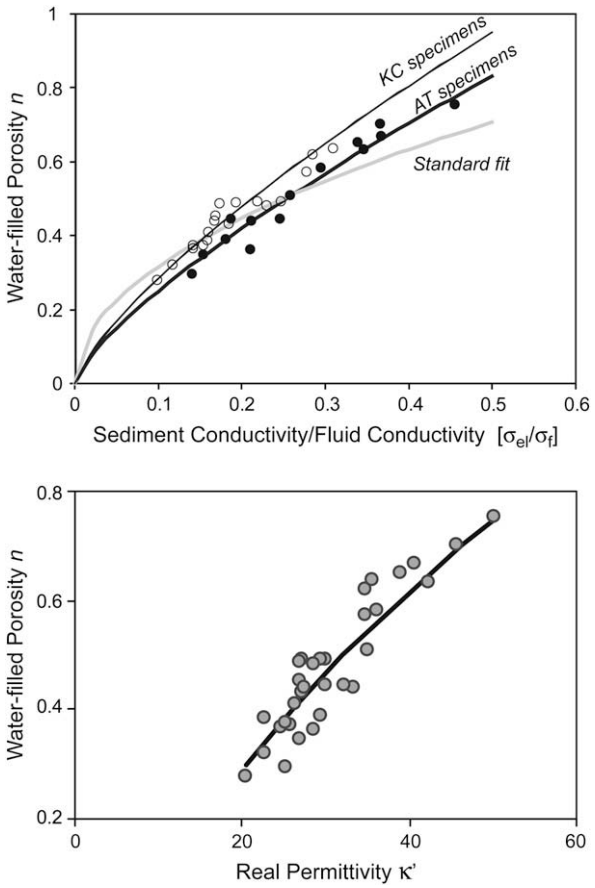

Fig. 10. Porosity as a function of conductivity ratios (Eq. 7) and real permittivity (Eq. 8) for experiments conducted at 1 GHz on six specimens lacking hydrate. Separate fits for the KC (open circles) and AT (filled circles) specimens are shown on the top panel, with parameters reported in the text. The gray curve on the top panel shows $n = (\sigma_{el}/\sigma_f)^{0.5}$, which reflects parameters closer to those used in Archie fits in the literature (e.g., Collett and Ladd, 2000; Jin et al., 2002). No distinction between the KC and AT data is made in the permittivity plot on the bottom panel.

$$r \approx \frac{w}{S_a \rho_w}, \tag{6}$$

where w denotes water content, and ρ_w is the mass density of pore fluid, here taken as $\rho_w = 1009$ kg m^{-3} for 20% THF–salt solution. The estimated pore size ranges from 2 to 5 nm for the KC specimens. The corresponding equilibrium temperature depression for pores of this size is −15 K to −36 K.

6.5. Estimating fluid-filled porosity and hydrate saturation

Estimations of fluid-filled porosity from real permittivity and electrical conductivity data can be robust when adequate material models are available. Here, we use permittivity and conductivity data gathered at the end of each consolidation stage to examine the relationship between these measurements and fluid-filled porosity. The goal of this analysis is to explore the use of these data to assess hydrate concentration in pore space, under the assumption that pore space within the hydrate stability zone must be filled either with fluid or gas hydrate.

Fig. 10 shows the relation between electrical measurements and porosity at the end of consolidation for all loading stages and for all specimens. A power-law Archie-type equation is used to fit the electrical conductivity data (Archie, 1942)

$$n = a\left(\frac{\sigma_{el}}{\sigma_f}\right)^{0.75}, \tag{7}$$

where σ_{el} is the specimen conductivity and σ_f is the pore fluid conductivity. The conductivities for pore fluid vary from 6 S m^{-1} to 20 S m^{-1} for salt concentration of 0.96–6 molal, respectively, during phase transformation. Salt concentration varies during phase transformation due to ion exclusion during hydrate formation. The coefficient a in Eq. (7) has a value of 1.6 for the KC specimens and 1.4 for the AT specimens.

A CRIM (Complex Refractive Index Method)-type model is adopted for the real permittivity data (Birchak et al., 1974)

$$n = \frac{\sqrt{\kappa'} - \sqrt{\kappa'_s}}{\sqrt{\kappa'_w} - \sqrt{\kappa'_s}}, \tag{8}$$

where κ' is the specimen permittivity, κ'_s represents soil particle permittivity, and κ'_w denotes pore fluid permittivity. For the 20% THF solution with salt concentration 0.96–6 molal, κ'_s is 5 and κ'_w varies from 58 to 38, respectively. The real permittivity of the mixture is mostly governed by porosity and the hydrate saturation and barely affected by pore fluid salinity.

These material models can be used to estimate the porosity filled with free water during phase transformation at constant effective stress and thus the gas hydrate saturation in pores. In the case of conductivity data, computations must also take into consideration ion exclusion and the changes in conductivity in the remaining fluid in closed systems. The difference between calculated S_{hyd} values with and without correction for ion exclusion varies according to porosity and can reach 0.1. The evolution in hydrate saturation S_{hyd} during formation and dissociation is estimated from the measured permittivity and conductivity. Using this approach, we estimated S_{hyd} during the phase transformation of the KC specimen under different applied vertical effective stress (Fig. 11). Comparable results were obtained by Sun and Goldberg (2005) in the Mackenzie Delta Mallik 5L-38 well using 1.1 GHz measurements on samples with real permittivity of 5–20, electrical conductivity of 0.1–0.5 S m^{-1} and inferred S_{hyd} of 20–95%.

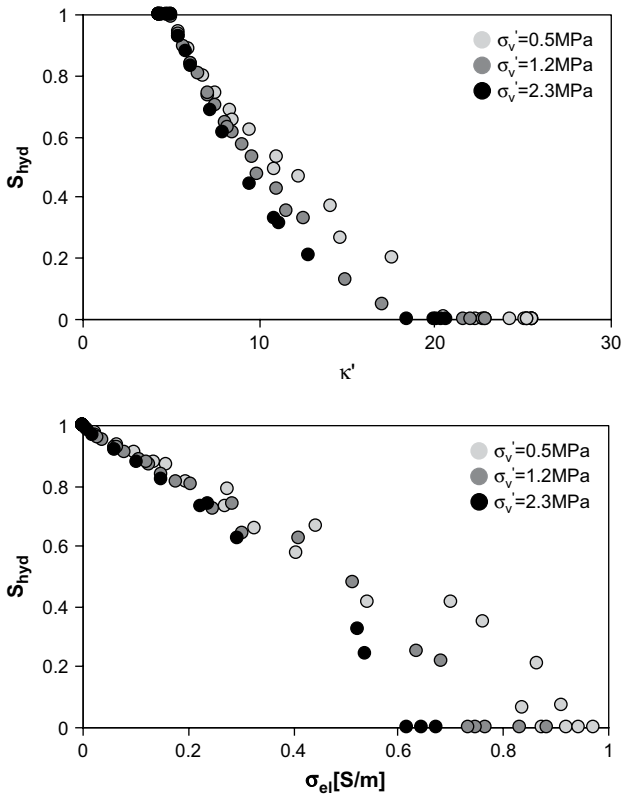

Fig. 11. Hydrate saturation in the pore space S_{hyd} estimated from real permittivity κ' and electrical conductivity σ_{el} measured on the remolded KC specimen with synthetic hydrate.

7. Conclusions

Consolidation experiments on undisturbed and remolded natural sediments obtained during drilling in potential gas hydrate zone in the northern Gulf of Mexico gas hydrates province and tested with and without synthetic hydrate reveal the following.

- The high compression index of these Gulf of Mexico sediments in the normally consolidated range reflects their high plasticity.
- Effective stress controls the stiffness of uncemented, normally consolidated sediments lacking hydrates. The sensitivity to the state of stress is high ($\beta = 0.3$–0.4), consistent with the high clay content and high plasticity of these sediments. In sediments with high concentration of synthetic hydrate, the effect of hydrates overrides the effect of effective stress on stiffness ($\beta \approx 0$).
- Phase transformation monitoring suggests the possibility of ion exclusion and an increase in ionic concentration in remaining pore fluids during hydrate formation, as previously documented in some field settings (e.g., Torres et al., 2004). This effect may have coupled with a gradual decrease in unfrozen pore size to further depress the equilibrium temperature.
- Decementation or skeletal debonding appears to be negligible when the 100% hydrate-filled sediments are unloaded from effective vertical stresses ranging from 1.2 to 2.3 MPa. Therefore, such specimens should experience limited sampling effects due to skeletal unloading. We caution that care should be taken to reload such samples to the in situ effective stress condition as soon as possible after retrieval. Complementary work not shown here has demonstrated significant decementation and debonding at 50% hydrate saturation (Lee, 2007). Therefore, it is only at very high hydrate saturations, which are likely rare in most natural settings, that sampling effects are relatively minimal.
- Permittivity in the microwave frequency range provides a good measure of free water volume fraction, while electrical conductivity indicates the availability and mobility of ions. Taken

together, these parameters are good indicators of the hydrate volume fraction. These methods of estimating hydrate volume fraction have potential applications for assessments of natural occurrences of gas hydrate.

Acknowledgments

This research was supported at Georgia Tech by the Joint Industry Project for Methane Hydrates, administered by Chevron with funding from award DE-FC26-01NT41330 from DOE's National Energy Technology Laboratory and by Goizueta Foundation funding to J.C.S. Comments by M. Lee and W. Waite improved the manuscript. C.R. thanks N. Toksöz for logistical support at MIT during completion of this work. Any use of a trade, product, or firm names is for descriptive purposes only and does not imply endorsement by the U.S. Goverment.

References

American Society of Testing and Materials (ASTM), 2003. Standard Test Method for One-dimensional Consolidation Properties of Soils, D 2435–03. American Society of Testing and Materials, Philadelphia.

Anderson, R., Llamedo, M., Tohidi, B., Burgass, R.W., 2003. Experimental measurement of methane and carbon dioxide clathrate hydrate equilibria in mesoporous silica. J. Phys. Chem. B 107, 3507–3514.

Archie, G.E., 1942. The electrical resistivity log as an aid in determining some reservoir characteristics. Petr. Trans. AIME 146, 54–62.

Birchak, J.R., Gardner, C.G., Hipp, J.E., Victor, J.M., 1974. High dielectric constant microwave probes for sensing soil moisture. Proc. IEEE 62 (1), 93–98.

Claypool, G.E., 2006. Gulf of Mexico Gas Hydrate Joint Industry Project (GOMJIP), 2005. The Cruise of the Drilling Vessel Uncle John, Mobile, Alabama to Galveston, Texas, Atwater Valley Blocks 13/14 and Keathley Canyon Block 151, 17 April to 22 May 2005. Available from: http://www.netl.doe.gov/technologies/oil-gas/publications/Hydrates/reports/GOMJIPCruise05.pdf.

Clennell, M.B., Hovland, M., Booth, J.S., Henry, P., Winters, W.J., 1999. Formation of natural gas hydrates in marine sediments, 1. Conceptual model of gas hydrate growth conditioned by host sediment properties. J. Geophys. Res. 104, 22985–23303.

Collett, T.S., Ladd, J., 2000. Detection of gas hydrate with downhole logs and assessment of gas hydrate concentrations (saturations) and gas volumes on the Blake Ridge with electrical resistivity log data. In: Paull, C.K., Matsumoto, R., Wallace, P.J., Dillon, W.P. (Eds.). Proc. ODP, Sci. Results, 164: College Station, TX (Ocean Drilling Program), pp. 179–191. doi:10.2973/odp.proc.sr.164.219.2000 <http://dx.doi.org/10.2973/odp.proc.sr.164.219.2000>.

Diegel, F.A., Karlo, J.F., Schuster, D.C., Shoup, R.C., Tauvers, P.R., 1995. Cenozoic structural evolution and tectono-stratigraphic framework of the northern Gulf Coast continental margin. In: Jackson, M.P.A., Roberts, D.G., Snelson, S. (Eds.). AAPG Memoir 65, 109–151.

Everett, D.H., 1961. Thermodynamics of frost damage to porous solids. Trans. Faraday Soc. 57, 1541–1551.

Francisca, F., Yun, T.S., Ruppel, C., Santamarina, J.C., 2005. Geophysical and geotechnical properties of near-seafloor sediments in the northern Gulf of Mexico gas hydrates province. Earth Planet. Sci. Lett. 237, 924–939.

Hyndman, R.D., Spence, G.D., 1992. A seismic study of methane hydrate marine bottom simulating reflectors. J. Geophys. Res. 97, 6683–6698.

Hutchinson, D.R., Hart, P.E., Ruppel, C.D., Snyder, F. and Dugan, B. Seismic and thermal characterization of a Bottom Simulating Reflection in the northern Gulf of Mexico. In: Collett, T.S., Johnson, A., Knapp, C., Boswell, R. (Eds.), Natural Gas Hydrates: Energy Resources, Potential and Associated Geologic Hazards. AAPG Special Publication, in press.

Hutchinson, D.R., Hart, P.E., Collett, T.S., Edwards, K.M., Twichell, D.C., Snyder, F., 2008. Geologic framework of the 2005 Keathley Canyon gas hydrate research well, northern Gulf of Mexico. Mar. Petr. Geol. 25, 906–918.

Jin, Y.K., Lee, M.W., Collett, T.S., 2002. Relationship of gas hydrate concentration to porosity and reflection amplitude in a research well, Mackenzie Delta, Canada, Mar. Petr. Geol. 19, 407–415.

Claypool, G.E., Robertson, G., 2008. Geochemical constraints on the origin of the pore fluids and gas hydrate distribution at Atwater Valley and Keathley Canyon, northern Gulf of Mexico. Mar. Petr. Geol. 25, 860–872.

Klein, K., Santamarina, J.C., 2003. Electrical conductivity in soils: underlying phenomena. J. Environ. Eng. Geophys. 8, 263–273.

Leaist, D.G., Murray, J.J., Post, M.L., Davidson, D.W., 1982. Enthalpies of decomposition and heat-capacities of ethylene-oxide and tetrahydrofuran hydrates. J. Phys. Chem. 86, 4175–4178.

Lee, J.Y., 2007. Hydrate-bearing Sediments: Formation and Geophysical Properties. Ph.D. thesis, Georgia Institute of Technology, 241 pp.

Lee, M., Collett, T., 2008. Integrated analysis of well logs and seismic data to estimate gas hydrate concentrations at Keathley Canyon, northern Gulf of Mexico. Mar. Petr. Geol. 25, 924–931.

Lee, J.S., Santamarina, J.C., 2005. Bender elements: performance and signal interpretation. J. Geotech. Geoenviron. Eng. 131, 1063–1070.

Lee, J.Y., Yun, T.S., Santamarina, J.C., Ruppel, C., 2007. Observations related to tetrahydrofuran and methane hydrate for laboratory studies of hydrate-bearing sediments. Geochem. Geophys. Geosys. 8, Q06003, doi:10.1029/2006GC001531.

Lide, D.R., 2003. CRC Handbook of Chemistry and Physics. CRC Press, Cleveland, Ohio, 2576 pp.

Lorenson, T.D., Claypool, G.E., Dougherty, J.A., 2008. Natural gas geochemistry of sediments drilled on the 2005 Gulf of Mexico JIP cruise. Mar. Petr. Geol. 25, 873–883.

Mullin, J.W., 2001. Crystallization. Butterworth-Heinemann, London, 594 pp.

Peel, F.J., Travis, C.J., Hossack, J.R., 1995. Genetic structural provinces and salt tectonics of the Cenozoic offshore U.S. Gulf of Mexico: a preliminary analysis. In: Jackson, M.P.A., Roberts, D.G., Snelson, S. (Eds.), AAPG Memoir, 65, pp. 109–151.

Santamarina, J.C., Klein, K.A., Fam, M.A., 2001. Soils and Waves. J. Wiley & Sons, New York, 488 pp.

Santamarina, J.C., Francisca, F., Yun, T.-S., Lee, J.-Y., Martin, A.I., Ruppel, C., 2004. Mechanical, Thermal, and Electrical Properties of Hydrate-bearing Sediments. AAPG Hedberg Abstracts Available from: http://www.searchanddiscovery.net/documents/abstracts/2004hedberg_vancouver/extended/santamarina/santamarina.htm.

Santamarina, J.C., Ruppel, C., 2008. The impact of hydrate saturation on the mechanical, electrical, and thermal properties of hydrate-bearing sand, silts, and clay, Proceedings of the 6th International Conference on Gas Hydrates, Vancouver, B.C. Canada, July 6–10, CD-ROM.

Sassen, R., Joye, S., Sweet, S.T., DeFreitas, D.A., Milkov, A.V., MacDonald, I.R., 1999. Thermogenic gas hydrates and hydrocarbon gases in complex chemosynthetic communities, Gulf of Mexico continental slope. Org. Geochem. 30, 485–497.

Sloan, E.D., 1998. Clathrate Hydrates of Natural Gases. Marcel Dekker, New York, 705 pp.

Sun, Y.F., Goldberg, D., 2005. Dielectric method of high-resolution gas hydrate estimation. Geophys. Res. Lett. 32, L04313, doi:10.1029/2004GL021976.

Torres, M.E., Wallmann, K., Trehu, A.M., Bohrmann, G., Borowski, W.S., Tomaru, H., 2004. Gas hydrate growth, methane transport, and chloride enrichment at the southern summit of Hydrate Ridge, Cascadia margin off Oregon. Earth Planet. Sci. Lett. 226, 225–241.

Winters, W.J., Dugan, B., Collett, T.S., 2008. Physical properties of sediments from Keathley Canyon and Atwater Valley, JIP Gulf of Mexico gas hydrate drilling program. Mar. Petr. Geol. 25, 896–905.

Wood, W., Hart, P.E., Hutchinson, D.R., Dutta, N., Snyder, F., Coffin, R.B., Gettrust, J.F., 2008. Gas and gas hydrate distribution around seafloor seeps in Mississippi Canyon, northern Gulf of Mexico, using multi-resolution seismic imagery. Mar. Petr. Geol. 25, 952–959.

Yun, T.S., Narsilio, G.A., Santamarina, J.C., 2006a. Physical characterization of core samples recovered from Gulf of Mexico. Mar. Petr. Geol. 23, 893–900.

Yun, T.S., Narsilio, G.A., Santamarina, J.C., Ruppel, C., 2006b. Instrumented pressure testing chamber for characterizing sediment cores recovered at in-situ hydrostatic pressure. Mar. Geol. 229, 285–293.

Yun, T.S., Santamarina, J.C., Ruppel, C., 2007. Mechanical properties of sand, silt, and clay containing tetrahydrofuran hydrate. J. Geophys. Res. 112, B04106, doi:10.1029/2006JB004484.

Zatsepina, O., Buffett, B.A., 2003. Nucleation of gas hydrate in marine environments. Geophys. Res. Lett. 30, doi:10.1029/2002GL016802.